

$K^+\Lambda(1520)$ photoproduction at forward angles near threshold with the BGOOD experiment

E.O. Rosanowski^{1,a}, T.C. Jude^{1,b}, S. Alef¹, A.J. Clara Figueiredo¹, R. Di Salvo², D. Elsner¹, A. Fantini^{2,3}, O. Freyermuth¹, F. Frommberger¹, F. Ghio^{4,5}, J. Groß¹, K. Kohl¹, P. Levi Sandri⁶, G. Mandaglio^{7,8}, R. Messi^{2,3}, D. Moricciani², P. Pedroni⁹, B.-E. Reitz¹, M. Romaniuk¹⁰, G. Scheluchin¹, H. Schmieden¹, and A. Sonnenschein¹

¹ Rheinische Friedrich-Wilhelms-Universität Bonn, Physikalisches Institut, Nußallee 12, 53115 Bonn, Germany

² INFN Roma “Tor Vergata”, Via della Ricerca Scientifica 1, 00133, Rome, Italy

³ Università di Roma “Tor Vergata”, Dipartimento di Fisica, Via della Ricerca Scientifica 1, 00133, Rome, Italy

⁴ INFN sezione di Roma La Sapienza, P.le Aldo Moro 2, 00185, Rome, Italy

⁵ Istituto Superiore di Sanità, Viale Regina Elena 299, 00161, Rome, Italy

⁶ INFN - Laboratori Nazionali di Frascati, Via E. Fermi 54, 00044, Frascati, Italy

⁷ INFN sezione Catania, 95129, Catania, Italy

⁸ Università degli Studi di Messina, Dipartimento MIFT, Via F. S. D’Alcontres 31, 98166, Messina, Italy

⁹ INFN sezione di Pavia, Via Agostino Bassi, 6 - 27100 Pavia, Italy

¹⁰ Institute for Nuclear Research of NASU, 03028, Kyiv, Ukraine

Received: date / Revised version: date

Abstract. The differential cross section for $\gamma p \rightarrow K^+\Lambda(1520)$ was measured from threshold to a centre-of-mass energy of 2090 MeV at forward angles at the BGOOD experiment. The high statistical precision and resolution in centre-of-mass energy and angle allows a detailed characterisation of this low-momentum transfer kinematic region. The data agree with a previous LEPS measurement and support effective Lagrangian models that indicate that the contact term dominates the cross section near threshold.

PACS. 13.60.Le Photoproduction of mesons 25.20.-x Photonuclear reactions

1 Introduction

Strangeness photoproduction is a crucial tool to understand baryon resonance spectra and the underlying degrees of freedom afforded in the low energy, non-perturbative regime of QCD. $K\Lambda^*$ and $K\Sigma^*$ photoproduction has frequently been used over the last twenty years to probe the third resonance region in attempts to characterise known higher mass N^* and Δ states and search for so called *missing resonances* which have been predicted by constituent quark models [1,2,3,4,5,6], lattice QCD calculations [7], and Dyson-Schwinger equations of QCD [8] but not observed experimentally in $N\pi$ final states [9,10]. $K\Lambda^*$ channels are unique in that the isoscalar Λ acts as an isospin filter, only permitting intermediate s -channel N^* resonances, and for the ground state Λ , the self-analysing weak decay enables easier access to baryon-recoil polarisation observables.

The Λ^* excitation spectrum however is itself poorly understood compared to the non-strange baryon sector, mainly due to a scarcity of experimental data [11]. Very few measurements on $S = -1$ resonances (both Λ^* and Σ^*

states) have been made over the last 20 years. The exception to this are measurements of the final states $K^+\Sigma^0\pi^0$ and $K^+\Sigma^+\pi^\pm$ [12,13,14,15,16] in both electro- and photoproduction, which have mainly been focussed on decays of the $\Lambda(1405)$. Studies of the $\Lambda(1405)$ are largely driven by its exotic nature and it is now considered the archetypal molecular-like hadron in the uds quark sector [17]. The large mass difference to the spin-orbit partner, the $\Lambda(1520)$ is also hard to explain within a CQM, and given the strong evidence of the molecular nature of the $\Lambda(1405)$, it is natural to question the structure of the $\Lambda(1520)$. Refs. [18,19,20], for example employed a chiral coupled channel model which described the $\Lambda(1520)$ as a quasi-bound state of $\pi\Sigma(1385)$ and $K\Xi(1530)$.

Previous measurements of $K^+\Lambda(1520)$ photoproduction near threshold have been performed at the LEPS [21] and CLAS [14,22] experiments¹, which have been supported by models employing effective Lagrangians [25,26]. The model of He and Chen [25] was able to describe the data by including the contact term, s -channel, u -channel and t -channel K and K^* exchanges. It was determined

¹ There are also earlier measurements made at 11 GeV at the SLAC spectrometer [23] and between 2.8 and 4.8 GeV from the LAMP2 collaboration [24].

^a Corresponding author: s6emrosa@uni-bonn.de

^b Corresponding author: jude@physik.uni-bonn.de

that the contact term dominates close to threshold, with $K^* t$ -channel contributions at higher centre-of-mass energies. Two N^* resonances with spins $3/2$ and $5/2$ were also required with masses close to 2.1 GeV for an adequate reproduction of the data. The LEPS collaboration also reported a bump like structure at a centre-of-mass energy of approximately 2.1 GeV. It was speculated that this may be due to either interference with the ϕp final state or alternatively an additional resonance. The angular distribution however did not support the introduction of a new resonance at this energy.

If the $\Lambda(1520)$ is a candidate for a molecular-like state, it is of interest to determine the dependency that momentum transfer has upon the differential cross section. It would be expected that a loosely bound system breaks up under large momentum transfer, which is observed for example, in coherent reactions off deuterium and light nuclei (see for example, Ref. [27]). Accessing forward K^+ angles close to threshold minimises the momentum transfer (minimising the Mandelstam variable, t) to the $\Lambda(1520)$, and an enhancement or structure may be expected if a meson-baryon type “resonating structure” contributes, for example, a molecular-type configuration. The BGOOD photoproduction experiment [28] at the ELSA facility [29,30] at the University of Bonn is ideally suited to measure associated strangeness in this kinematic regime. The K^+ can be identified at forward angles in the *Forward Spectrometer*, while the hyperon decays almost isotropically, the decay products of which are identified in the central region with the *BGO Rugby Ball* electromagnetic calorimeter. The BGOOD collaboration is pursuing a programme of strangeness photoproduction measurements under low-momentum transfer conditions [16,31,32] which have not been achievable with high statistical precision at other facilities. An example of the importance of measuring this region is the measured forward differential cross section for $K^+ \Sigma^0$, where a cusp-like structure was observed at the $K^+ \Sigma(1385)$ threshold [32,33]. The measurement of $K^+ \Lambda(1520)$ photoproduction close to threshold at forward angles is therefore the mandatory next step in order to understand the role of potential molecular-like structure in the strangeness sector.

2 Experimental setup and analysis procedure

BGOOD, shown in Fig. 1, is comprised of two main parts: a central calorimeter region, ideal for neutral meson identification, and a magnetic *Forward Spectrometer* for charged particle identification and momentum reconstruction (for a detailed description see Ref. [28]). The *BGO Rugby Ball* is the main detector over the central region, covering laboratory polar angles 25 to 155° . The detector is comprised of 480 BGO crystals for the reconstruction of photon momenta via electromagnetic showers in the crystals. The separate time readout per crystal enables a clean separation and identification of neutral meson decays. Between the BGO Rugby Ball and the target are the *Plastic Scintillating Barrel* for charged particle identification via $\Delta E - E$

techniques and the *MWPC* for charged particle tracking and vertex reconstruction.

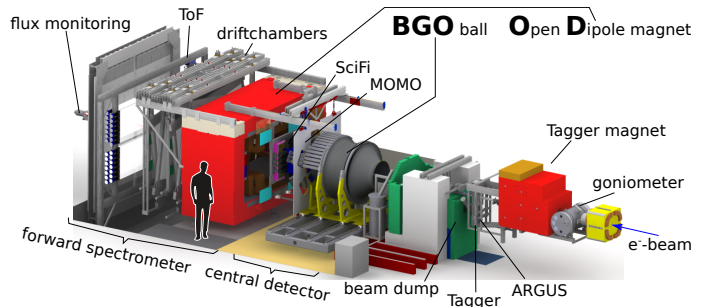


Fig. 1. The BGOOD experimental setup. Figure originally shown in Ref. [28].

The Forward Spectrometer covers a laboratory polar angle 1 - 12° . The tracking detectors, *MOMO* and *SciFi* are used to track charged particles from the target. Downstream of these is the *Open Dipole Magnet* operating at an integrated field strength of 0.216 Tm. A series of eight double layered *Drift Chambers* track charged particles after curvature of their trajectories in the magnetic field and are used to determine particle momenta with a resolution of approximately 6% .² Three *Time of Flight (ToF) Walls* downstream of the drift chambers determine particle β and are used in combination with the measured momentum for particle identification via mass determination. Track reconstruction in the Forward Spectrometer is described in Ref. [28].

The small intermediate region between the central region and the Forward Spectrometer is covered by *SciFi*, which consists of three concentric rings, each with 32 plastic scintillators for charged particle detection.

The presented results are from data taken over two periods. The first dataset was taken in 2017 and used a 6 cm long liquid hydrogen target with a 3.2 GeV electron beam over 22 days, resulting in an integrated photon flux of 1.11×10^{12} over the photon energy range 1650 to 1850 MeV (the region of the presented data). The second dataset taken in 2018 used an 11 cm long liquid hydrogen target with a 2.8 GeV electron beam over 18 days, resulting in an integrated photon flux of 7.28×10^{11} over the photon energy range 1650 to 1850 MeV. Four different hardware triggers were implemented to ensure the data can be used a variety of measurements (see Refs. [28,31]), however the results presented here required a single trigger combination, which was an incident photon registered in the photon tagger and a minimum energy deposition of 150 MeV in the BGO Rugby Ball.

K^+ were identified in the Forward Spectrometer by reconstructing their invariant mass from the momentum and β measurements. K^+ candidates were selected over a 2σ range of the reconstructed mass. This increased lin-

² The resolution improves to 3% if the Open Dipole Magnet is operating at the maximum integrated field strength of 0.432 Tm.

early with K^+ momentum, ranging from $45 \text{ MeV}/c^2$ to $73 \text{ MeV}/c^2$ at momenta 450 and $1000 \text{ GeV}/c$ respectively.

Two different topologies of the final state were required for consistency checks and to constrain systematic uncertainties. The first required only a K^+ candidate in the Forward Spectrometer, and the second required an additional π^0 to be identified in the BGO Rugby Ball via the decay, $\pi^0 \rightarrow \gamma\gamma$. π^0 candidates were selected where the $\gamma\gamma$ invariant mass was within 30 MeV of the nominal π^0 mass (corresponding to 2σ). The requirement of the π^0 reduces the dataset to candidate events where the decays, $K^+(\Lambda(1520)) \rightarrow \Sigma^0\pi^0$ and $K^+(\Lambda(1520)) \rightarrow \Lambda\pi^0\pi^0$ are observed.

The event yields contained background from hadronic reactions, where either the forward K^+ was misidentified from the large background of π^+ and e^+ , or other associated strangeness reactions of K^+Y and $K^+Y\pi$ were selected instead of $K^+\Lambda(1520)$. This background can be observed in histograms of the missing mass recoiling from the K^+ in the final state. Three examples for different centre-of-mass energy (W) intervals are shown in Fig. 2 for the two different topologies (a K^+ candidate with or without an additional π^0 candidate). To extract the $K^+\Lambda(1520)$ yields, these were fitted with distributions from simulated associated strangeness channels. This was achieved using the BGOOD GEANT4 [34] simulation, including all spatial, energy and time resolutions, magnetic fields and hardware efficiencies (see Ref. [28] for details). Event distributions were based on measured data where available or phase distributions, however the small W and $\cos\theta_{\text{CM}}^K$ range per interval made differences in distributions negligible. Signal events ($K^+\Lambda(1520)$) and background from $K^+\Lambda$, $K^+\Sigma^0$, $K^+\Sigma^0(1385)$ and $K^*\Lambda$ were simulated. $K^+\Lambda(1405)$ was not included due to the mass degeneracy to the $\Sigma(1385)$. From previous studies [31], it was realised that $\Delta\pi^+$ was required as it gave substantial background contribution from $K^+-\pi^+$ misidentification, however this only contributes at lower missing mass than the $\Lambda(1520)$ signal. An additional background distribution from misidentifying either π^+ or e^+ as K^+ was determined by repeating the analysis but requiring a negatively charged track (a technique first used in Refs. [31,32]). This resulted in π^- and e^- distributions which appeared (by eye) identical to their positively charged counterparts. The measured data extends only to the $K^*\Sigma^0$ threshold as the missing mass distribution from this background channel was too close to the $K^+\Lambda(1520)$ distribution for a reliable separation of signal and background.³

The detection efficiency was determined by simulating $K^+\Lambda(1520)$ events assuming a phase space distribution, including the known $\Lambda(1520)$ decay branching ratios. Shown in Fig. 3, the detection efficiency when only requiring a K^+ has a maximum of approximately 12%, whereas the requirement of an additional π^0 lowers the efficiency to approximately 3%. The small differences between the

³ Preliminary measurements of K^*Y channels at BGOOD have been made and are under analysis for future publications. Once complete, it is the intention to subtract the $K^*\Sigma^0$ contributions and extend the measured $K^+\Lambda(1520)$ W range.

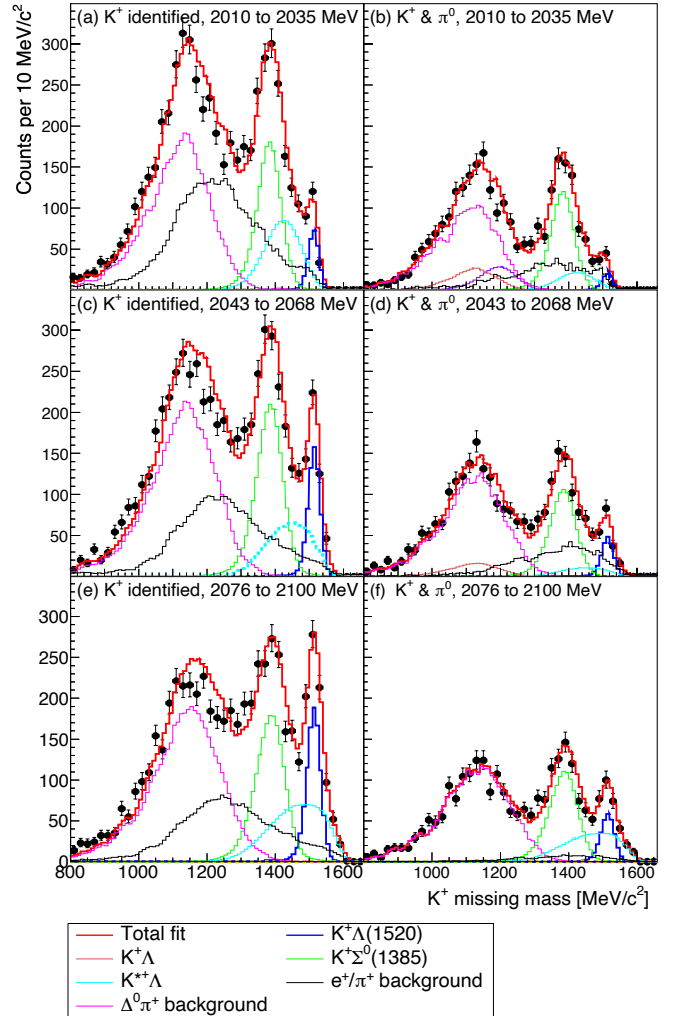


Fig. 2. Examples from the 2018 dataset of the missing mass recoiling from the K^+ for the two topologies for different W intervals labelled inset. Left panels are for when only a forward K^+ candidate is required and right panels are for when an additional π^0 candidate is required. Each W interval corresponds to two tagger channels. The fitted distributions from simulated data (and real data for the $e^+\pi^+$ background described in the text) are listed in the legend.

two datasets is due to the different target lengths and the efficiency of hardware triggers.

Most of the systematic uncertainties listed in Table 1 were calculated for previous publications using the same datasets [31]. To determine the systematic uncertainty of the yield extraction from the fitting to the K^+ missing mass spectra, the differential cross section for the two datasets and the two different selection criteria were determined (shown in Fig. 4). An uncertainty of 5% was estimated by comparing the measurements. The total systematic uncertainty, when summed in quadrature is 9.3%.

The results presented in the next section only required the K^+ detection (no π^0) to improve statistical precision and is an error weighted combination of both datasets.

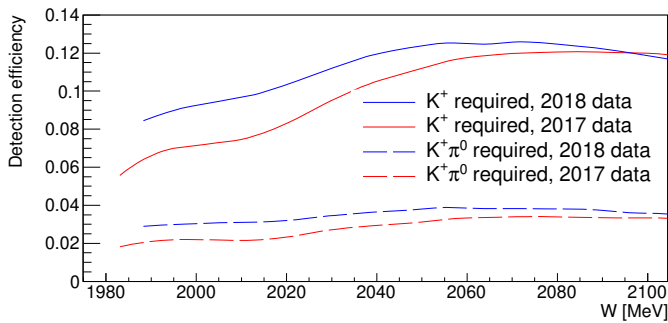


Fig. 3. The detection efficiency for $\cos \theta_{\text{CM}}^K > 0.9$ for the two different datasets and either requiring only a forward K^+ or an additional π^0 in the BGO Rugby Ball.

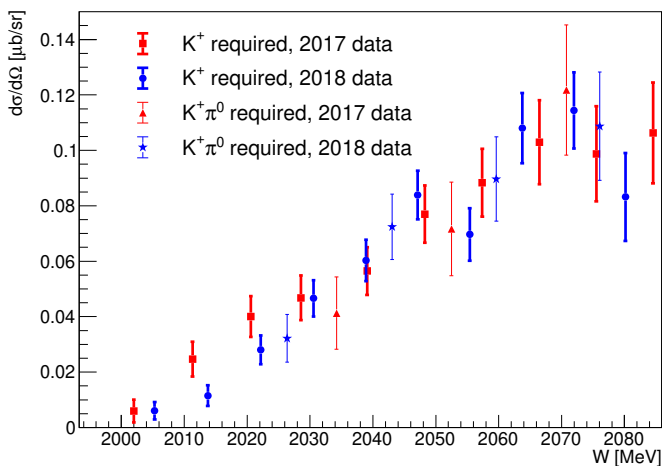


Fig. 4. The differential cross section for $\cos \theta_{\text{CM}}^K > 0.9$ for the two different datasets and either requiring only a forward K^+ or an additional π^0 in the BGO Rugby Ball (labelled inset). The intervals in W is either every photon tagger or every two photon tagger channels when requiring just the K^+ or the $K^+ \pi^0$ combination respectively.

3 Results and interpretation

The differential cross section for $\cos \theta_{\text{CM}}^K > 0.9$ is shown in Fig. 5 (filled black circles). The data provide the first measurements with high precision close to threshold, achieving a resolution in W of approximately 10 MeV which is 2.5 times finer than previous LEPS data [21] with similar statistical precision. Superimposed is the effective Lagrangian model of He and Chen [25] which was fitted to the LEPS data. There is a good agreement to the model calculation, with a reduced χ^2 of 1.96 when only including the statistical errors, however when combining the systematic and statistical errors in quadrature, a reduced χ^2 of 1.04 is achieved. The data support the case for the contact term to dominate the cross section close to threshold.

The $\cos \theta_{\text{CM}}^K$ resolution of approximately 0.02 permits binning in finer $\cos \theta_{\text{CM}}^K$ intervals. Fig. 6 shows the same dataset in $\cos \theta_{\text{CM}}^K$ intervals of 0.033. No significant change is observed across this $\cos \theta_{\text{CM}}^K$ range, which is in contrast, for example, to the $K^+ \Sigma^0$ differential cross sec-

Source	% error
Beam spot alignment	4.0
Photon flux	4.0
K^+ selection	2.0
SciFi efficiency	3.0
Target wall contribution	2.0
Track time selection	2.0
Target length	0.9
ToF wall efficiency	1.5
MOMO efficiency	1.0
Drift chamber efficiency	1.0
Beam energy calibration	1.0
Modelling of hardware triggers	1.0
Forward track geometric selection	1.0
Fitting K^+ missing mass spectra	5.0
Summed in quadrature	9.3

Table 1. Systematic uncertainty contributions.

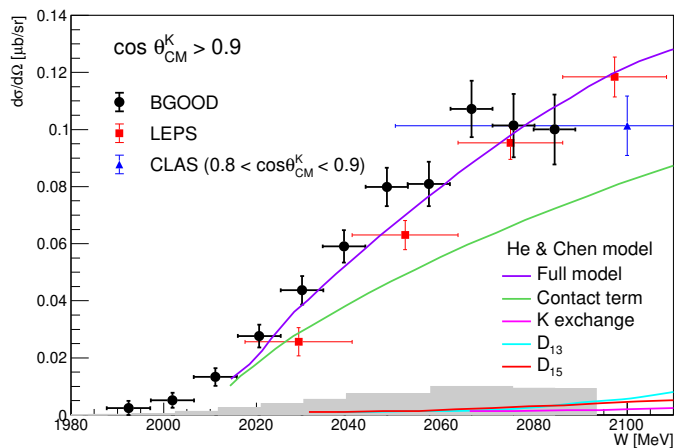


Fig. 5. The differential cross section for $\cos \theta_{\text{CM}}^K > 0.9$ for the combined BGOOD data set requiring only a forward K^+ (filled black circles with systematic errors indicated as the filled grey area on the abscissa). Previous LEPS [21] and CLAS data [14] are shown as filled red squares and filled blue triangles respectively. For all data, vertical bars indicate statistical error and horizontal bars indicate the range of the data point. The CLAS data covers a $\cos \theta_{\text{CM}}^K$ range of 0.8 to 0.9. The results from the effective Lagrangian model of He and Chen [25] are superimposed and labelled inset.

tion which exhibits a cusp-like structure becoming more prominent in the most forward interval [32]. This fine binning in $\cos \theta_{\text{CM}}^K$ provides an accurate means to extrapolate the data to the minimum possible momentum transfer to the $\Lambda(1520)$. This is defined in terms of the Mandelstam variable, $t = (p_\gamma - p_K)^2$, where p_γ and p_K are the four-momenta of the photon beam and K^+ respectively. To account for the distribution of t within each two dimensional W and $\cos \theta_{\text{CM}}^K$ interval, a generated distribution was used based on the measured differential cross section. For each interval in W and $\cos \theta_{\text{CM}}^K$, the mean average value of t was used as the central value, and the width was determined as $\sqrt{12}$ RMS. A fixed mass of the $\Lambda(1520)$ was assumed for the calculation in order to remove long

tails to very high and very small t . For each W interval, the minimum momentum transfer, t_{\min} was calculated, which corresponds to $\cos \theta_{\text{CM}}^K = 1$. Fig. 7 shows examples of the differential cross section with respect to $|t - t_{\min}|$ for three different W intervals.

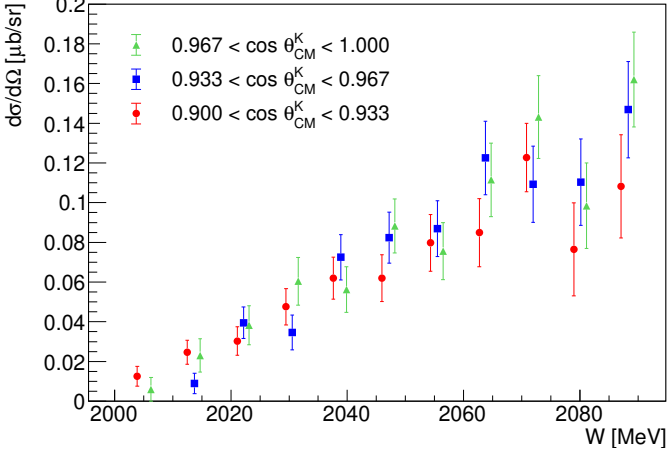


Fig. 6. The differential cross section for fine intervals of $\cos \theta_{\text{CM}}^K > 0.9$. Only the statistical error are shown. The data points are staggered -1 , 0 and $+1$ MeV around the mean W for clarity.

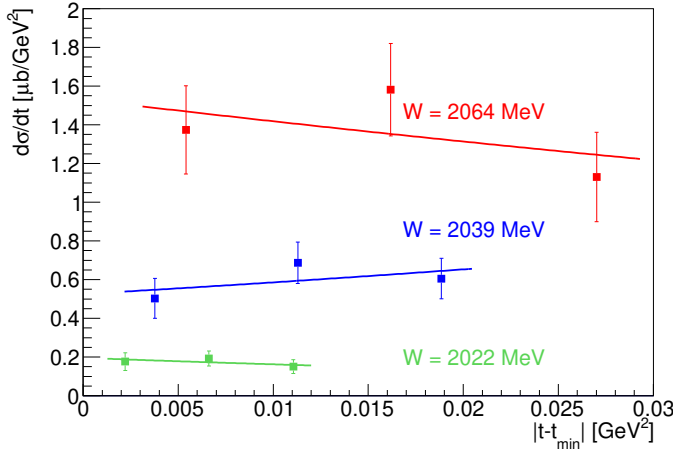


Fig. 7. The differential cross section with respect versus $|t - t_{\min}|$ for three example intervals of W (only the statistical error shown). Equation 3 has been fitted separately to each W interval, indicated by the colour coded lines.

The differential cross section at t_{\min} was determined for each W interval by fitting the function in Eq. (1):

$$\frac{d\sigma}{dt} = \left. \frac{d\sigma}{dt} \right|_{t=t_{\min}} e^{S|t-t_{\min}|} \quad (1)$$

Fig. 8(a) shows the extrapolated differential cross section at t_{\min} . The slope parameter, S is shown in Fig. 8(b). Within limited statistical precision it appears to remain

flat. This is consistent with the contact term dominating near threshold, as was proposed by the effective Lagrangian model of He and Chen [25]. If K or K^* t -channel exchange was to dominant for example, the differential cross section would be expected to be more forward peaked, resulting in a negative value for S .

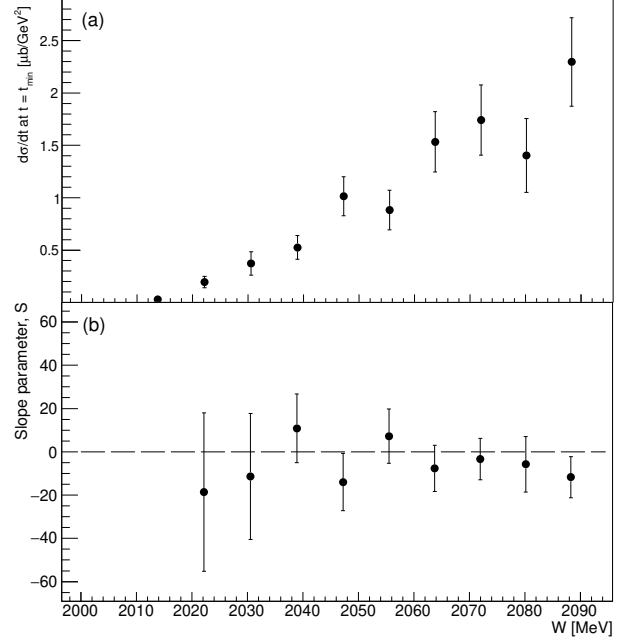


Fig. 8. (a) The differential cross section, $d\sigma/dt$ extrapolated to t_{\min} versus W . (b) The slope parameter, S (in Eq. (1)) versus W .

4 Conclusions

The differential cross section for $\gamma p \rightarrow K^+ \Lambda(1520)$ was measured for $\cos \theta_{\text{CM}}^K > 0.9$ from threshold to a centre-of-mass energy of 2090 MeV at the BGOOD experiment. The resolution in both W and $\cos \theta_{\text{CM}}^K$ enable a precise characterisation in this kinematic regime for the first time. The data are consistent with the previous data of LEPS [21] and the effective Lagrangian model of He and Chen [25].

Acknowledgements

We thank the staff and shift-students of the ELSA accelerator for providing an excellent beam.

This work is supported by the Deutsche Forschungsgemeinschaft Project Numbers 388979758 and 405882627 and the Third Scientific Committee of the INFN. This publication is part of a project that has received funding from the European Union's Horizon 2020 research and innovation programme under grant agreement STRONG-2020 No. 824093.

References

1. S. Capstick and N. Isgur. *Phys. Rev. D*, 34:2809, 1986.
2. S. Capstick. *Phys. Rev. D*, 46(2846), 1992.
3. S. Capstick and W. Roberts. *Phys. Rev. D*, 49:4570, 1994.
4. D. O. Riska and G. E. Brown. *Nucl. Phys. A*, 679:577, 2001.
5. E. Klempt and J. M. Richard. *Rev. Mod. Phys.*, 82:1095, 2010.
6. E. Klempt and B.Ch. Metsch. *Eur. Phys. J. A*, 48:127, 2012.
7. R. G. Edwards, J. J. Dudek, D. G. Richards, and S. Wallace. *Phys. Rev. D*, 84:074508, 2011.
8. H. L. L Roberts, L. Chang, I. C. Cloët, and C. D. Roberts. *Few-Body Systems*, 51:51, 2011.
9. S. Capstick and W. Roberts. *Prog. Part. Nucl. Phys.*, 45:S241.
10. U. Löring, B. C. Metsch, and H. R. Petry. *Eur. Phys. J. A*, 10:395, 2001.
11. P. A. Zyla, et al. (Particle Data Group). *Prog. Theor. Exp. Phys.*, page 083C01, 2020.
12. H. Y. Lu, et al. (CLAS Collaboration). *Phys Rev. C*, 88:045202, 2013.
13. K. Moriya, R. A. Schumacher, et al. (CLAS Collaboration). *Phys. Lett. C*, 87:035206, 2013.
14. K. Moriya, et al. (CLAS Collaboration). *Phys. Rev. C*, 88:045201, 2013.
15. M. Niiyama, et al. (LEPS Collaboration). *Phys. Rev. C*, 78:035202, 2008.
16. G. Scheluchin, T. C. Jude, et al. (BGOOD Collaboration). *Phys. Lett. B*, 833:137375, 2022.
17. F.-K. Guo, C. Hanhart, U.-G. Meißner, Q. Wang, Q. Zhao, and B.-S. Zou. *Rev. Mod. Phys.*, 90:015004–1, 2018.
18. E. E. Kolomeitsev and M. F. M. Lutz. *Phys. Lett. B*, 585(243), 2004.
19. S. Sarkar, E. Oset, and M. J. Vicente Vacas. *Nucl. Phys. A*, 750:294, 2005.
20. S. Sarkar, E. Oset, and M. J. Vicente Vacas. *Phys Rev. C*, 72:015206, 2005.
21. H. Kohri, et al. (LEPS Collaboration). *Phys. Rev. Lett.*, 104:172001, 2010.
22. U. Shrestha, T. Chetry, C. Djalali, K. Hicks, S. I. Nam, et al. (CLAS Collaboration). *Phys. Rev. C*, 103:025206, 2021.
23. A. M. Boyarski et al. *Phys. Lett.*, 34B:547, 1971.
24. D. P. Barber et al. *Z. Phys. C*, 7:17, 1980.
25. J. He and X.-R. Chen. *Phys. Rev. C*, 86(035204), 2012.
26. S.-I. Nam, A. Hosaka, and H.-C. Kim. *Phys. Rev. D*, 71:114012, 2005.
27. B. Krusche. *Eur. Phys. J. Special Topics*, 198:199, 2011.
28. S Alef, et al. (BGOOD Collaboration). *Eur. Phys. J. A*, 56:104, 2020.
29. W. Hillert. *Eur. Phys. J. A*, 28:139, 2006.
30. W. Hillert et al. *EPJ Web Conf.*, 134:05002, 2017.
31. S. Alef, et al. (BGOOD Collaboration). *Eur. Phys. J. A*, 57:80, 2021.
32. T. C. Jude, et al. (BGOOD Collaboration). *Phys. Lett. B*, 820:136559, 2021.
33. T. C. Jude et al. *J. Phys.: Conf. Ser.*, 2586:012003, 2022.
34. J. Allison et al. *Nucl. Instrum. Meth. A*, 835:186, 2016.